https://doi.org/10.5194/egusphere-2025-4142
Preprint. Discussion started: 10 September 2025

Impacts of Air–sea Coupling on Systematic Errors in Medium-Range Winter Forecasts over the North Pacific and North Atlantic

Tien-Yiao Hsu[1], Matthew R. Mazloff[2], Sarah T. Gille[2], Hai Lin[3], K. Andrew Peterson[3], Rui Sun[2], Aneesh C. Subramanian[4], and Luca Delle Monache[1]

[1]Center for Western Weather and Water Extremes, Scripps Institution of Oceanography, University of California, San Diego, La Jolla, California, United States
[2]Scripps Institution of Oceanography, University of California, San Diego, La Jolla, California, United States
[3]Meteorological Research Division, Environment and Climate Change Canada (ECCC), Dorval, Québec, Canada
[4] Department of Atmospheric and Oceanic Sciences, University of Colorado Boulder, Boulder, Colorado, United States

Correspondence: Tien-Yiao Hsu (tienyiao@ucsd.edu)

Abstract.

The impact of air–sea coupling in North Pacific and North Atlantic medium-range forecasts during winter is assessed using 20 years (1998–2017) of hindcasts produced by the Global Ensemble Prediction System (GEPS) of Environment and Climate Change Canada (ECCC). We compare an uncoupled atmospheric model (versions 5, GEPS5) with an atmosphere–ocean coupled model (version 6, GEPS6) alongside European Centre for Medium-Range Weather Forecasts Reanalysis v5 (ERA5) as the verification dataset. We find that by the third pentad, or days 11–15, coupling weakens the Aleutian Low, the Icelandic Low, and the Atlantic Subtropical High. This produces less integrated vapor transport (IVT) over the Pacific and Atlantic Oceans, whose spatial patterns are modulated by phases of Madden–Julian oscillation (MJO). Coupling also results in colder sea surface temperature (SST) over the Kuroshio Current Extension region and produces a weaker Aleutian Low due to less upward latent heat fluxes. The weaker Aleutian Low further reinforces its weakening through a positive feedback loop. Lastly, the air–sea coupling reduces the latent heat flux bias variance by 10–20%, thus improving the IVT.

1 Introduction

The improvement of medium-range forecasts (5–15 days) remains critical to better prepare society for weather extremes. The time-evolving ocean states are a crucial element needed to correctly simulate strong weather variability, such as the Madden–Julian Oscillation (MJO; Madden and Julian, 1971; Wheeler and Hendon, 2004) and atmospheric rivers (ARs; Gimeno et al., 2014), that are important signals in subseasonal-to-seasonal (S2S) precipitation forecasts (Subramanian et al., 2019). Mid-latitude cyclones can cause strong sea surface temperature (SST) perturbations (Hsu et al., 2024) approximately 10 days after passage (Kobashi et al., 2019) and feed back to the storm tracks (Booth et al., 2012). Major weather agencies have adopted high-resolution (less than 50 km) coupled systems for medium-range forecasts and have shown detectable improvement in

https://doi.org/10.5194/egusphere-2025-4142
Preprint. Discussion started: 10 September 2025

forecast skill through the use of coupled models (Brassington et al., 2015). The benefit often comes from the tropics, where cloud convection is an important source of available potential energy and is sensitive to SST.

Since air–sea fluxes are modulated by near-surface wind speed, two-way air–sea coupling measurably improves tropical cyclone forecasts. The SST cooling induced by wind-driven ocean mixed-layer deepening and Ekman upwelling can feed back in a few days to reduce storm intensity (Rainaud et al., 2017; Smith et al., 2018; Sun et al., 2022; Polichtchouk et al., 2025). Similarly, coupling is also known to have a positive impact on MJO prediction (DeMott et al., 2015; Savarin and Chen, 2022) because SST cooling due to wind anomalies and the diurnal variation of mixed-layer depth can modulate MJO propagation speed and intensity. The ability to predict the MJO is particularly important because it is known to remotely modulate the North Atlantic Oscillation (NAO) (Cassou, 2008; Lin et al., 2009; Scaife et al., 2017) and to influence global temperature and precipitation on a subseasonal timescale (Stan et al., 2017).

Coupled models have advanced to grid sizes of less than a degree, leading to new understandings of air–sea coupling. In particular, there is a growing awareness of the role of ocean-eddy-scale air–sea interactions in high-resolution simulations where the SST gradients can effectively modify near-surface atmospheric curl, divergence, and therefore heat fluxes (Small et al., 2008; Bishop et al., 2017; Liu et al., 2021; Seo et al., 2023; Renault et al., 2024). However, over western boundary current extensions coupled models do not necessarily predict the SST within eddies better than persistence (Vellinga et al., 2020), contributing to systematic errors in medium-range forecasts.

In this study, we focus on the impact of air–sea coupling in the North Pacific and North Atlantic during the winter. We take advantage of archived hindcasts of the Global Ensemble Prediction System (GEPS) versions 5 (GEPS5) and 6 (GEPS6) of the Environment Climate Change Canada (ECCC) provided as part of the subseasonal-to-seasonal (S2S) project (Vitart et al., 2017). Because GEPS5 is run with prescribed sea surface conditions and GEPS6 with interactive sea surface conditions from a coupled ocean model, their contrasts reveal the impact of air–sea coupling. The global models can see the full impact of air–sea coupling, a potential advantage over regional models, where the coupling effects are constantly removed as the air keeps flowing in from the prescribed lateral boundary conditions. We use integrated vapor transport (IVT; Rutz et al., 2014) as a proxy to assess weather extremes due to its connection with atmospheric rivers (ARs; Zhu and Newell, 1994; Gimeno et al., 2014; Rutz et al., 2014; Guan and Waliser, 2015; Pasquier et al., 2019; Waliser and Guan, 2017). Overall, we find three main points. First, the coupling weakens the Aleutian Low, the Icelandic Low, and the Atlantic Subtropical High, subsequently resulting in a weaker IVT whose spatial pattern is influenced by the MJO. Second, the coupling simulates a colder SST over the Kuroshio Current extension, generating a weaker Aleutian Low, which further weakens itself through a positive feedback loop. Third, the air–sea coupling reduces the latent heat flux bias variance by 10–20% and improves the IVT forecast over the Kuroshio Current Extension.

In Section 2, we introduce our datasets and methodology. Section 3 presents and discusses our results. In Section 4, we draw conclusions.

https://doi.org/10.5194/egusphere-2025-4142
Preprint. Discussion started: 10 September 2025

2 Dataset and Methods

2.1 GEPS

GEPS5 uses the Global Environmental Multiscale (GEM) atmospheric model (Côté et al., 1998b, a). GEPS5 has 45 vertical levels using log-pressure vertical coordinate (Girard et al., 2014), and uses the Ying–Yang grid with a horizontal resolution of 39 km (Qaddouri and Lee, 2011). As for the ocean boundary condition, GEPS5 uses the persistent anomaly method: on top of the climatological seasonal cycle, the 30-day average SST anomaly preceding the initial date is added and persists throughout the integration (Lin et al., 2016). The sea ice cover is adjusted according to local SST so that the resulting sea ice cover and SST are consistent (Gagnon et al., 2014). The initial conditions are obtained using an Ensemble Kalman-filter (EnKF; Houtekamer et al., 2009, 2014), with a digital filter (Fillion et al., 1995) and incremental analysis updates (Bloom et al., 1996) to reduce the shock during data assimilation (Deng et al., 2018).

GEPS6 is built on top of GEPS5 by replacing the simple statistical SST and sea ice model with a dynamical ocean and sea ice model. The ocean model is the Nucleus for European Modelling of the Ocean (NEMO) version 3.6 (Madec, 2008). NEMO uses z-level vertical coordinates, with hydrostatic, Boussinesq approximations, and a linear free surface. This version has a horizontal resolution of 0.25° ORCA grid (Bernard et al., 2006, a global tripolar grid configured to remove singularity of poles of a sphere) and 50 levels increasing from 1 m at the surface to 500 m at the deepest level. The sea ice model is the Los Alamos multi-category Community Ice Model version 4 (CICE4; Hunke, 2001; Lipscomb et al., 2007; Hunke et al., 2015). The initial conditions are obtained using the EnKF, with European Centre for Medium-Range Weather Forecasts hybrid (ECMWF-hybrid) gain applied to recenter ensemble members around the means of EnKF analysis and 4DEnVar analysis (Penny, 2014; Houtekamer et al., 2019). The 4DEnVar is a 4-dimensional variational data assimilation using the Global Deterministic Prediction System (Buehner et al., 2015; Lin et al., 2019).

For more detailed documentation, see Peterson et al. (2022) and Smith et al. (2018). Ensemble methods are described by Deng et al. (2018) for GEPS5 and Lin et al. (2019) for GEPS6.

2.2 Hindcast Data

The S2S project provides up to 60 lead days hindcasts (Vitart et al., 2008, 2017) from 13 different meteorological agencies. ECCC has contributed hindcast data from GEPS5 and GEPS6 from 1998–2017.

The hindcasts are produced on a weekly basis for GEPS5 and GEPS6. For each hindcast date, hindcasts corresponding to the same date were generated for 20 years 1998–2017. Each hindcast has a lead time of 32 days with 4 ensemble members. For GEPS6, the hindcast is generated such that it has twice as many start dates as the GEPS5 hindcast, as documented in Tables S1 and S2. We subsample the GEPS6 hindcast by choosing the closest start date (underlined in Table S2) to GEPS5. This strategy minimizes the impact of the start time difference and ensures that the GEPS6 subset has the same amount of data as GEPS5. In our focus months, December, January, and February, the start dates of GEPS5 are exactly one day later than GEPS6.

As our verification dataset, we use European Centre for Medium-Range Weather Forecasts (ECMWF) Reanalysis v5 (ERA5; Hersbach et al., 2020). In the Pacific and Atlantic Oceans, it can well capture offshore diurnal SST cycles under various wind

https://doi.org/10.5194/egusphere-2025-4142
Preprint. Discussion started: 10 September 2025

conditions (Yao et al., 2021). Over Europe, the wind variability is skillfully predicted (Molina et al., 2021; Chen et al., 2024). Over North America, Chen et al. (2024) shows that ERA5 has skills over wind and precipitation associated with extra-tropical cyclones, with a tendency to underestimate high winds and overestimate low winds. A study over the Red Sea shows ERA5 is challenged by land–sea induced local dynamics (Alkhalidi et al., 2025).

2.3 Assessment of air–sea coupling

Ideally, the effect of air–sea coupling can be revealed by taking the difference between coupled and uncoupled hindcasts. However, GEPS5 and GEPS6 do not share common start times. Therefore, we reference both fields to ERA5 by computing the difference between GEPS and ERA5 data and then sorting the runs by start month. We first define the pentad bias

$$\beta_{\mathrm{pdt},X}\left(\boldsymbol{r},t_s,p,\gamma\right)=\left(\Delta w\right)^{-1}\int_{t_l=(p-1)\ \Delta w}^{p\ \Delta w}X_{\mathrm{pdt,hcst}}\left(\boldsymbol{r},t_s,t_l,\gamma\right)-X_{\mathrm{ref}}\left(\boldsymbol{r},t_s+t_l\right)\ \mathrm{d}t_l, \tag{1}$$

where $\beta_{\mathrm{pdt},X}$ is the bias of the hindcast product "pdt" of the variable X at location $\boldsymbol{r}$, t_s is the start time, t_l is the lead time, p is the lead pentad (starting from 1), γ is the ensemble member of a total N_γ members, and $\Delta w = 5$ day is the size of the pentad. The subscript "hcst" denotes the hindcast, "ref" denotes the reference dataset that is used to verify the hindcast, i.e., ERA5 in this paper. With the $\langle\cdot\rangle$ being the spatial averaging over a region S, we can separate the bias into a spatial mean $\langle\beta_{\mathrm{pdt},X}\rangle$ and an anomaly $\beta'_{\mathrm{pdt},X}=\beta_{\mathrm{pdt},X}-\langle\beta_{\mathrm{pdt},X}\rangle$. The averaged bias variance can then be written as the sum of mean and patterned variances. That is,

$$\left\langle\beta^2_{\mathrm{pdt},X}\right\rangle=\overbrace{\left\langle\beta_{\mathrm{pdt},X}\right\rangle^2}^{\text{mean}}+\overbrace{\left\langle\beta'^2_{\mathrm{pdt},X}\right\rangle}^{\text{patterned}}. \tag{2}$$

Later in the text for the sake of simplicity, we define bias variance $\epsilon_{\mathrm{pdt},X}=\left\langle\beta^2_{\mathrm{pdt},X}\right\rangle$, mean bias variance $\overline{\epsilon}_{\mathrm{pdt},X}=\left\langle\beta_{\mathrm{pdt},X}\right\rangle^2$, and patterned bias variance $\tilde{\epsilon}_{\mathrm{pdt},X}=\left\langle\beta'^2_{\mathrm{pdt},X}\right\rangle$, with the decomposition as $\epsilon_{\mathrm{pdt},X}=\overline{\epsilon}_{\mathrm{pdt},X}+\tilde{\epsilon}_{\mathrm{pdt},X}$.

The bias and its variance decomposition of variable X of a product pdt grouped by start time set ϕ is

$$B_{\mathrm{pdt},X}\left(\boldsymbol{r},\phi,p\right)=\left\{\beta_{\mathrm{pdt},X}\left(\boldsymbol{r},t_s,p,\gamma\right)\mid t_s\in\phi,\gamma=1,\ldots,N_\gamma\right\}, \tag{3a}$$

$$E_{\mathrm{pdt},X}\left(S,\phi,p\right)=\left\{\epsilon_{\mathrm{pdt},X}\left(S,t_s,p,\gamma\right)\mid t_s\in\phi,\gamma=1,\ldots,N_\gamma\right\}, \tag{3b}$$

$$\overline{E}_{\mathrm{pdt},X}\left(S,\phi,p\right)=\left\{\overline{\epsilon}_{\mathrm{pdt},X}\left(S,t_s,p,\gamma\right)\mid t_s\in\phi,\gamma=1,\ldots,N_\gamma\right\}, \tag{3c}$$

$$\tilde{E}_{\mathrm{pdt},X}\left(S,\phi,p\right)=\left\{\tilde{\epsilon}_{\mathrm{pdt},X}\left(S,t_s,p,\gamma\right)\mid t_s\in\phi,\gamma=1,\ldots,N_\gamma\right\}, \tag{3d}$$

To test the significance, the degrees of freedom are counted by making the following two assumptions: (a) output from different start times or different ensembles is independent, and (b) the output within the same pentad is not independent. In both GEPS5 and GEPS6, during 1998–2017 there are 4 start times in January with 4 ensemble members. Therefore, for each pentad there are $20\times4\times4=320$ degrees of freedom.

To assess the impact of air–sea coupling as a function of space, we define bias change

$$\Delta B_X\left(\boldsymbol{r},\phi,p\right)=\mu\left[B_{\mathrm{GEPS6},X}\left(\boldsymbol{r},\phi,p\right)\right]-\mu\left[B_{\mathrm{GEPS5},X}\left(\boldsymbol{r},\phi,p\right)\right], \tag{4a}$$

https://doi.org/10.5194/egusphere-2025-4142
Preprint. Discussion started: 10 September 2025

where μ is the averaging operator over a given set. A significance test is performed with the above-mentioned degrees of freedom.

2.4 Separation of MJO impact

To evaluate MJO impact, we define three start time groups using the outgoing-longwave-radiation (OLR)-based MJO index (OMI; Kiladis et al., 2014), a two-dimensional vector whose values are normalized principal components. When the magnitude of OMI is less than 1, the MJO is classified as inactive. When the magnitude of OMI is larger than 1, the MJO is active, and the MJO phases 1–8 are defined according to the phase angle of OMI. MJO phase contains spatial information of MJO: during MJO phases 1–4, the MJO convection center resides over the Indian Ocean. During MJO phases 5–8, the center is over the Maritime continent and tropical Pacific. The MJO start time groups are defined as

$$\phi_{\text{NonMJO}} = \{t \mid t \in \phi_{\text{DJF}} \text{ and the MJO is inactive more than half of the time in the next 15 days.}\} \tag{5a}$$

$$\phi_{\text{P1234}} = \{t \mid t \in \phi_{\text{DJF}}, \text{ the MJO is in phases 1–4 more than half of the time in the next 15 days.}\} \tag{5b}$$

$$\phi_{\text{P5678}} = \{t \mid t \in \phi_{\text{DJF}}, \text{ the MJO is in phases 5–8 more than half of the time in the next 15 days.}\} \tag{5c}$$

where ϕ_{DJF} is the set of all start times during December–January–February. The remaining start times are ambiguous, meaning that either the MJO is neither consistently inactive nor active, or the phase of MJO cannot be classed in either P1234 or P5678. Out of 1805 days of DJF during 1998–2017, there are 455 days of NonMJO, 331 days of P1234, 321 days of P5678, and 698 days that are ambiguous. (See Figure S1 for histogram.)

3 Results

3.1 Systematic Impact of Air–Sea Coupling On SST and Circulation

We compute the bias change ΔB, i.e., the difference between GEPS6 and GEPS5, of SST, 850 hPa geopotential height Z_{850}, and 500 hPa geopotential height Z_{500} of pentads 1–3 and present them in Figure 1. The black boxes in Figure 1c define the Kuroshio Current Extension (150°E–130°W, 30°–50°N) and the Gulf Stream (75°–15°W, 35°–55°N) regions, and the magenta boxes in Figures 1f and 1i define the Aleutian Low (140°E–130°W, 40°–60°N), Icelandic Low (30°W–20°E, 55°–70°N), and Atlantic Subtropical High (60°W–20°E, 20°–50°N) regions.

Throughout all pentads, the pattern of SST bias is consistent, with increased magnitude in later time (Figures 1a–c). Over the North Pacific, the SST is colder in GEPS6, with the alternating signs around coastal Japan signifying the error in simulating the KC. We see a similar cold bias in the North Atlantic, but with a strong northward shift of the Gulf Stream along 45°N. The impact of this shift extends northward all the way to the edge of Arctic sea ice.

As for the circulation, by pentad 3, Z_{850} shows a weakening in the Aleutian Low, the Icelandic Low, and the Atlantic Subtropical High (Figures 1f and 1i). The weakening of the Aleutian Low starts in pentad 1 and grows until pentad 3. The weakening of Icelandic Low starts remotely in the middle of Eurasia as a positive anomaly in pentad 1. Then, the anomaly

https://doi.org/10.5194/egusphere-2025-4142
Preprint. Discussion started: 10 September 2025

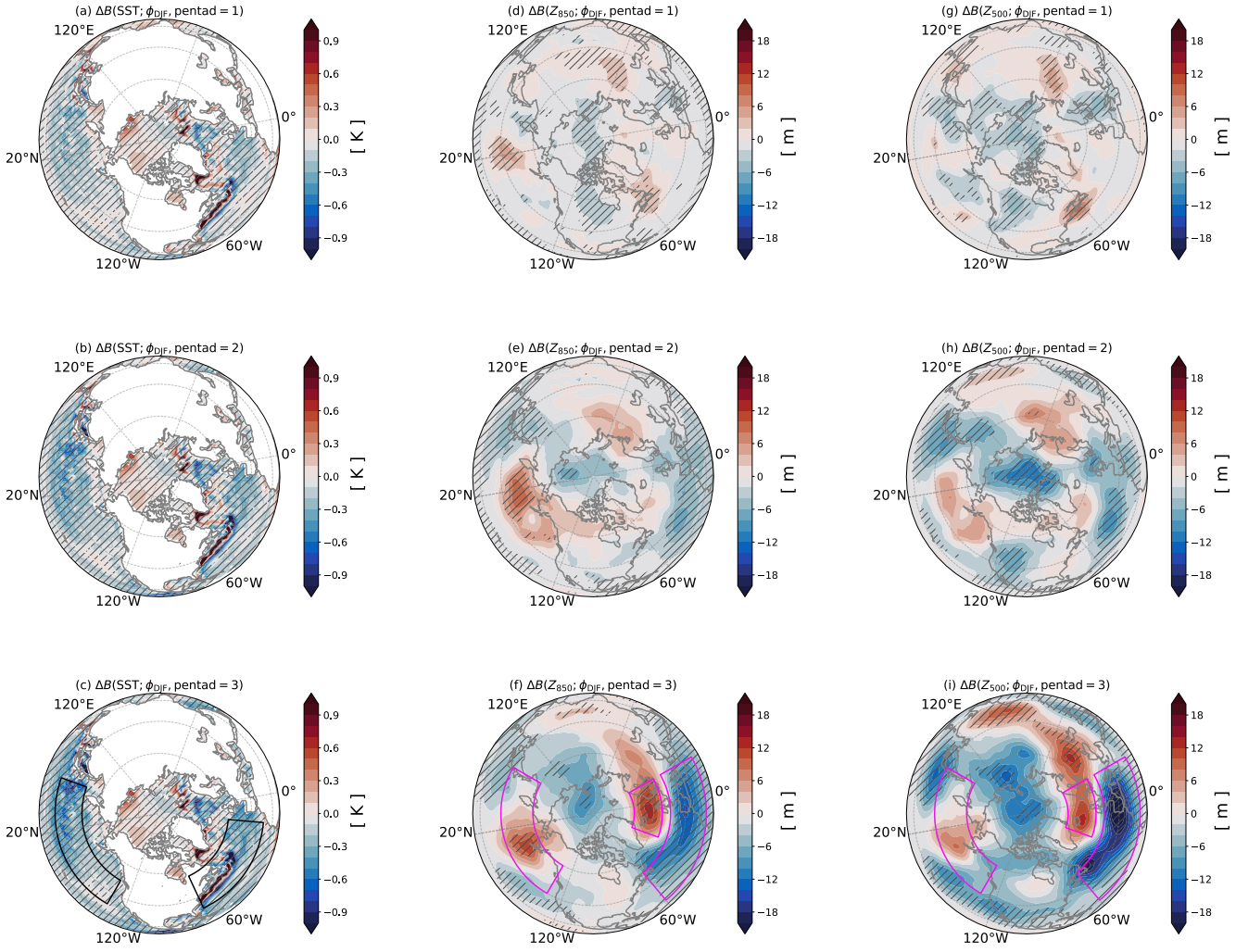

Figure 1. Bias changes ΔB of atmosphere quantities computed from Global Ensemble Forecast System (GEPS) version 5 (GEPS5) to GEPS version 6 (GEPS6) during December–January–February of the first three pentads in hindcast years 1998–2017. (a)–(c) ΔB of the sea surface temperature (SST) of pentad $= 1, 2,$ and 3. (d)–(f) Same as a–c but for 500 hPa geopotential height Z_{850}. (g)–(i) Same as (a)–(c) but for 500 hPa geopotential height Z_{500}. The hatched area passes the significance test of a p-value of 0.1. The black boxes in panel c define the Kuroshio Current Extension (150°E–130°W, 30°–50°N) and Gulf Stream (75°–15°W, 35°–55°N) regions, and the magenta boxes in panels f and i define the Aleutian Low (140°E–130°W, 40°–60°N), Icelandic Low (30°W–20°E, 55°–70°N), and Atlantic Subtropical High (60°W–20°E, 20°–50°N) regions.

grows and moves westward into the location of the Icelandic Low. Meanwhile, the weakening of the Atlantic Subtropical
145 High emerges in pentad 2, and its magnitude becomes comparable to the weakening of the Icelandic Low. Together with the

https://doi.org/10.5194/egusphere-2025-4142
Preprint. Discussion started: 10 September 2025

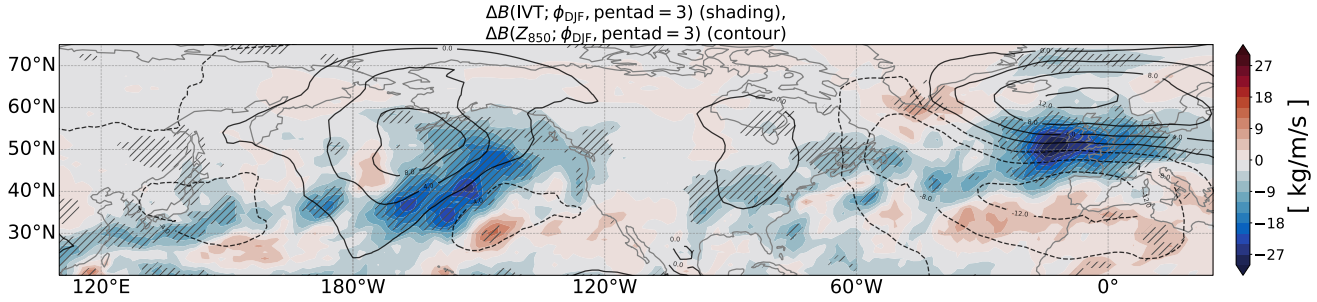

Figure 2. Bias changes ΔB of the integrated vapor transport (IVT, shading) and 850 hPa geopotential height Z_{850} (contours, spacing is 2 meters, and contours with negative values are dashed)) computed from Global Ensemble Forecast System (GEPS) version 5 (GEPS5) to GEPS version 6 (GEPS6) during December–January–February of the first three pentads in hindcast years 1998–2017. The hatched area means the IVT anomalies pass the significance test of a p-value of 0.1.

weakened Icelandic Low, the westerly winds in between (45°–60°N) decelerate. This deceleration is not restricted to the lower atmosphere but extends to Z_{500} (Figures 1g–i).

The Aleutian Low weakening appears to be linked to a similar Icelandic Low weakening through a Rossby wave train (Hoskins and Karoly, 1981; Karoly, 1983). As shown in Figures 1f and 1i, Z_{850} and Z_{500} reveal an alternating pattern of high and low centers, extending from the Aleutian Low through the Arctic to the Icelandic Low. The wave train pattern is more significant in Z_{850} than Z_{500}, suggesting that the impact originates from the lower atmosphere.

The large northward shift of the Gulf Stream directly forces Z_{850} and Z_{500}. Figures 1d and 1g show that there are positive geopotential anomalies at $45°\mathrm{N}, 75°\mathrm{W}$. The anomalies persist throughout pentads 1–2.

3.2 Systematic Impact of Air–Sea Coupling on Integrated Vapor Transport (IVT)

Here, we define $\mathrm{IVT} = \left| g^{-1} \int_{200\mathrm{hPa}}^{1000\mathrm{hPa}} q\, \boldsymbol{v}\, \mathrm{d}p \right|$. Figure 2 shows the bias change ΔB of the IVT (shading) and Z_{850} (contours) for pentad 3. Over the North Pacific, the IVT is reduced along the southeastern side of the weakened Aleutian Low towards the Gulf of Alaska. Over the North Atlantic, the reduced IVT lies between the weakened Icelandic Low and the Atlantic Subtropical High, with a more zonal orientation toward western Europe.

The shape of IVT bias depends on the MJO. Figures 3a–c show the composite bias changes of IVT (shading) and Z_{850} (contour) grouped by MJO-inactive, MJO phase 1–4, and MJO phase 5–8 as defined in Section 2.4. The weakened Aleutian Low remains in the middle of the North Pacific, such that the weakened Pacific IVT is consistently oriented southwest–northeast. In contrast, the Icelandic Low and Atlantic Subtropical High weakening is spatially more variable, such that the Atlantic IVT pattern is less consistent among MJO groups.

https://doi.org/10.5194/egusphere-2025-4142
Preprint. Discussion started: 10 September 2025

3.3 What Causes the Aleutian Low Weakening?

In this section, the goal is to understand the physical mechanisms that cause changes in the Aleutian Low. From Figures 3a–c, we know that the weakening bias is consistently simulated in GEPS6 relative to GEPS5, regardless of whether its shape is modulated by the MJO phase. This is an indication that local air–sea coupling is an important driver for the Aleutian Low weakening.

To remove the MJO influence, we examine the response of Z_{850} and latent heat fluxes H_{lat} composited with non-MJO groups. In the absence of MJO, the Aleutian Low weakens in GEPS6 relative to GEPS5 during pentads 1–2 (contours in Figures 4a–d). The SST bias change between 30°–60°N is -0.2 K in the first pentad, indicating that the coupling results in a colder SST (Figure 4a shading). This results in a reduction in H_{lat} (Figure 4c shading), causing a weaker cyclogenesis such that the Z_{850} is positively biased.

The Aleutian Low experiences a positive feedback loop where its initial weakening leads to further intensification of this weakening, primarily through interactions between circulation and H_{lat}. In particular, notice that the magnitude of the reduction in H_{lat} is larger at the southern flank of the Z_{850} anomaly because its anomalous circulation blows against the mean westerlies (Figure 4c). As previously demonstrated, the reduction of H_{lat} leads to a weaker Aleutian Low, resulting in stronger anomalous circulation in the next pentad (Figure 4d). This mechanism is a positive feedback.

3.4 Two-way Coupling Improves Latent Heat Fluxes and IVT Prediction

We use error variances as functions of lead pentads over the Kuroshio Current Extension and Gulf Stream regions to assess how coupling benefits prediction, as shown in Figures 5a–j. In the Kuroshio Current Extension region, GEPS6 performs better than GEPS5 in terms of the mean SST variance, but has poorer performance in patterned SST variance (Figure 5a). The patterned SST variance hindcast gradually reaches the mean ERA5 SST variance 0.60 ± 0.16 K (zonally detrended and area weighted variance, years 1998–2017 DJF). In GEPS6, the SST error is largely due to the hindcast initialization strategy of initializing with a monthly average Ocean Reanalysis Pilot 5 (ORAP5; Zuo et al., 2017) product. These errors are not representative of the impact of coupling, nor of SST error in the hindcast, which is shown to be improved in GEPS6 compared to GEPS5 (Lin et al., 2019, Figure 24). The use of a monthly products for initializing sea ice in the hindcast similarly leads to a large SST error signal along the Arctic sea ice.

Interestingly, in the Kuroshio Current Extension region the latent heat flux H_{lat}, GEPS6 outperforms GEPS5 in both mean and patterned variances (Figure 5b), and the error variance E of GEPS6 is 10–20% smaller than that of GEPS5. Because GEPS6 produces a less accurate SST but a better latent heat flux, this contrast highlights the importance of two-way coupling in correctly predicting air–sea fluxes, especially those associated with extra-tropical cyclones (Kobashi et al., 2019; Hsu et al., 2024). The improvement of H_{lat} subsequently leads to a better integrated water vapor (IWV, defined as $\mathrm{IWV} = g^{-1} \int_{200\mathrm{hPa}}^{1000\mathrm{hPa}} q \, \mathrm{d}p$) and therefore better IVT hindcast in GEPS6 (Figures 5c and d). In contrast, while air–sea coupling modifies Z_{850} (Figure 1a–c), it does not produce a better Z_{850} hindcast (Figure 5e).

https://doi.org/10.5194/egusphere-2025-4142
Preprint. Discussion started: 10 September 2025

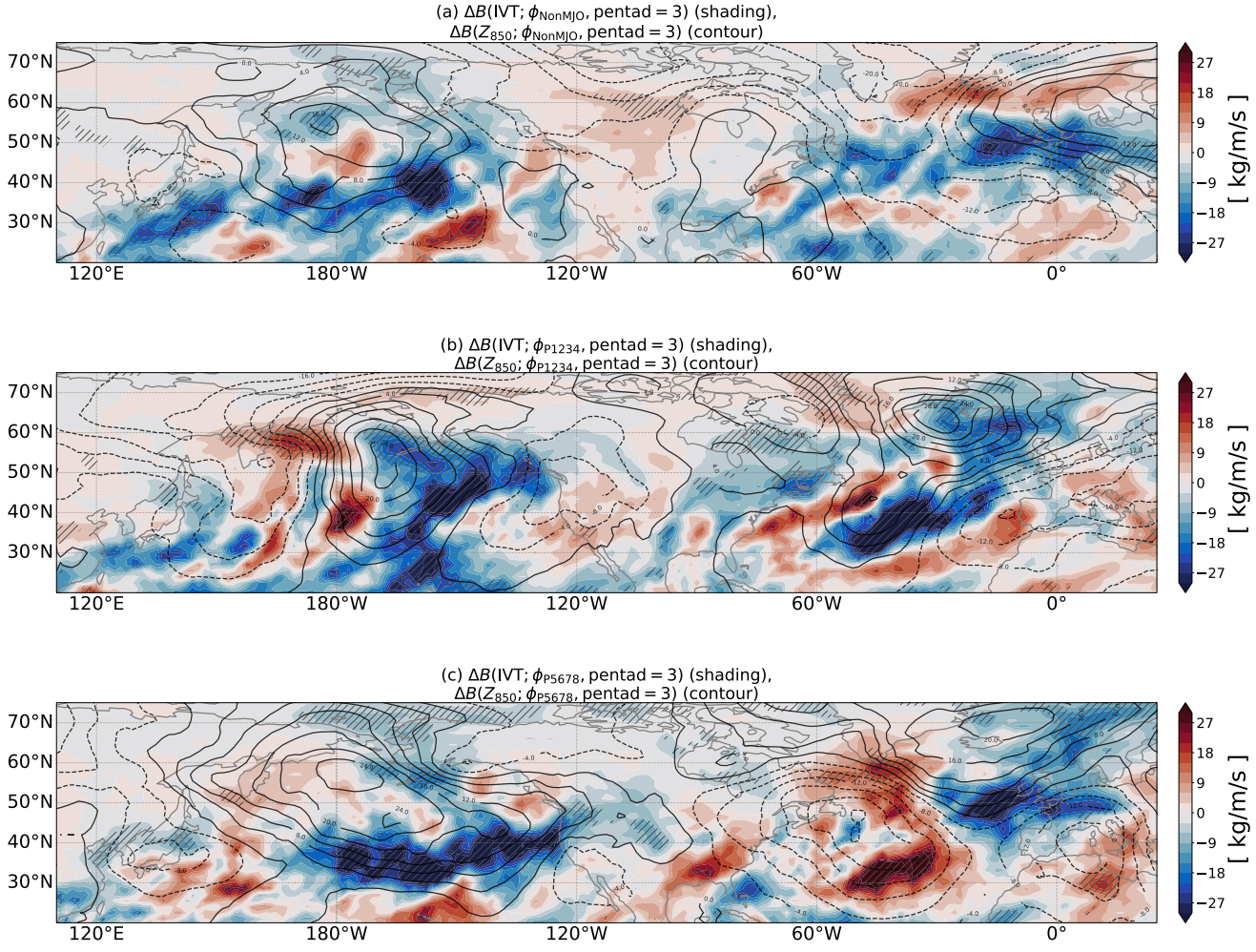

Figure 3. Bias changes ΔB of the integrated water vapor (IVT, shading) and 850 hPa geopotential height Z_{850} (contours, spacing is 2 meters, and contours with negative values are dashed) from Global Ensemble Forecast System (GEPS) version 5 (GEPS5) to GEPS version 6 (GEPS6) of the third pentad $p = 3$ in different start time groups in hindcast years 1998–2017 during December–January–February. (a) Non-MJO group. (b) P1234 group. (c) P5678 group. The hatched area means the IVT bias change passes the significance test of a p-value of 0.1.

In the Gulf Stream region, GEPS6 simulates a better mean variance of SST bias in the first three pentads. On the contrary, because GEPS6 simulates a northward-shifted Gulf Stream, there is a strong patterned variance of SST bias (Figure 5f). This signal propagates into patterned variance of H_{lat} bias (Figure 5g), resulting in little or no improvement in IWV and IVT (Figures 5h–i). Moreover, similar to the Kuroshio Current Extension region, we do not see a notable difference in Z_{850} (Figure 5j).

https://doi.org/10.5194/egusphere-2025-4142
Preprint. Discussion started: 10 September 2025

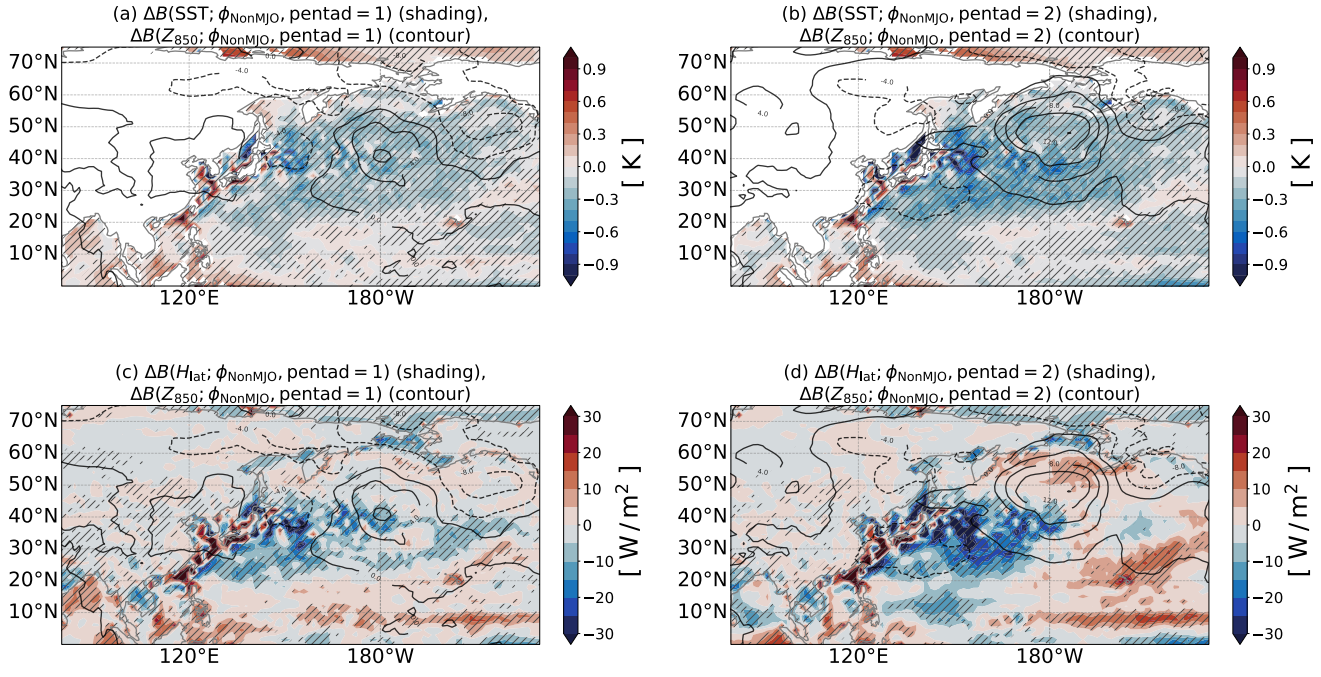

Figure 4. Bias change ΔB of the sea surface temperature (SST), upward latent heat flux (H_{lat}), and the 850 hPa geopotential height Z_{850} from Global Ensemble Forecast System (GEPS) version 5 (GEPS5) to GEPS version 6 (GEPS6) during Madden–Julian–Oscillation (MJO) inactive start time (ϕ_{NonMJO}) of the first two $p = 1, 2$ in hindcast years 1998–2017. (a) The shading is the $\Delta B_{\mathrm{SST}}\,(\phi_{\mathrm{NonMJO}}, p = 1)$. The contours are the $\Delta B_{Z_{850}}\,(\phi_{\mathrm{NonMJO}}, p = 1)$. The hatched areas are the location where $\Delta B_{H_{\mathrm{SST}}}$ passes the significance test of a p-value of 0.15. (b) Same as (a) but for $p = 2$. (c) Same as (a) but the shading and dotted-hatch are for the $\Delta B_{H_{\mathrm{lat}}}\,(\phi_{\mathrm{NonMJO}}, p = 1)$. (d) Same as (c) but for $p = 2$.

4 Discussion: The Role of Kuroshio Current Extension and the Gulf Stream

The Kuroshio Current Extension is an eddy-rich area where mesoscale (200 km and less) SST fronts modify the near-surface atmospheric convergence, curl, and thus air–sea fluxes in the marine atmosphere boundary layer (MABL) (Bishop et al., 2017; Seo et al., 2023; Renault et al., 2024). Our results show that the bias of SST over Kuroshio Current Extension leads to an Aleutian Low positive feedback response, implying that better Aleutian Low prediction can be achieved through optimizing the initialization. This will lead to better forecasts of the North Pacific jet and IVT, both of which are indicators for AR activities (Winters, 2021; Higgins et al., 2024).

The role of the Gulf Stream is less clear. While its persistent impact on Z_{850} is visible (Figure 3d–f), and the major atmospheric response over the Atlantic Ocean is immediately downstream of the Gulf Stream, the response does not emerge until the second pentad. Therefore, while the shift of the Gulf Stream may lead to the dipole patterns of Z_{850} and Z_{500} over the Atlantic Ocean, this signal is mixed with remote impacts. Future numerical studies are needed to gain a deeper understanding.

https://doi.org/10.5194/egusphere-2025-4142
Preprint. Discussion started: 10 September 2025

5 Conclusion

This study, using 20 years of hindcast data from ECCC's GEPS5 and GEPS6 alongside ERA5 reanalysis, demonstrates that air–sea coupling can impact medium-range wintertime forecasts over the North Pacific and North Atlantic.

The analysis of hindcast bias shows that the air–sea coupling results in a weaker Aleutian Low, Icelandic Low, and Atlantic Subtropical High within 15 days, leading to a weaker IVT over the northeastern Pacific and Atlantic. We also notice a possible teleconnection from the Aleutian Low through the Arctic into Icelandic Low via a Rossby wave train. Furthermore, the MJO phase can influence the resulting spatial distribution of IVT difference, suggesting its importance in tropical–extratropical interactions.

We investigated the cause of the weaker Aleutian Low due to air–sea coupling and found a physical mechanism. The coupling simulates a colder SST centered on the Kuroshio Current Extension, which reduces the latent heat flux. This leads to weaker cyclogenesis and thus a weaker Aleutian Low. The anomalous circulation that blows against the westerlies over the Kuroshio Current Extension further reduces the latent fluxes, creating a positive feedback loop that reinforces the initial bias.

When evaluating the bias variance, we find that the coupled model produces a slight degradation in SST hindcast, but a significant 10–20% less latent heat flux bias variance over the Kuroshio Current Extension compared to the uncoupled model. The improvement in latent heat flux explains the better IWV and thus the IVT hindcast. The IVT improvement is also more significant when the MJO is active. In the Gulf Stream, the northward shift bias is too strong such that the latent heat fluxes, and thus IWV and IVT, are not improved.

In conclusion, we find that optimizing the air–sea fluxes parameterization can lead to tangible improvements in medium-range forecasts in the Pacific and potentially the Atlantic. Moreover, the accurate representation of the Gulf Stream may improve the Atlantic circulation bias in the atmosphere.

Finally, this research highlights two potential future directions. First, regional simulations over the North Atlantic can be performed to isolate the influence of the Atlantic from the Pacific (Cassou, 2008). Second, there is a need for more physical understanding of how two-way coupling produces better air–sea fluxes. This potentially can mitigate the SST error along the Kuroshio Current Extension and the Gulf Stream that can tangibly force the atmosphere through modifying air–sea fluxes (Seo et al., 2023).

Code and data availability. The code used to generate the figures in this study has been deposited in https://github.com/meteorologytoday/paperfigures-airsea-cpl-ECCC. The data used to generate figures in this study have been deposited in Zenodo (https://doi.org/10.5281/zenodo.16938865). The GEPS5 and GEPS6 output can be obtained from ECMWF S2S Data Repository (https://apps.ecmwf.int/datasets/data/s2s-realtime-daily-averaged-cwao/)

Author contributions. Conceptualization, T.-Y.H.; Funding and resource acquisition, all authors; Investigation, T.-Y.H.; Project administration, T.-Y.H.; Visualization, T.-Y.H.; Writing–original draft, T.-Y.H.; Writing–review and editing, all authors.

https://doi.org/10.5194/egusphere-2025-4142
Preprint. Discussion started: 10 September 2025

Competing interests. Authors confirm that there are no competing interests present.

Acknowledgements. The authors would like to acknowledge support from CW3E through the California Department of Water Resources funded Atmospheric River Program Phase IV (contract number 4600014942). Authors acknowledge NOAA grants NA21OAR4310257 and NA22OAR4310597. M.R.M. acknowledges support from NASA award 80NSSC23K0979. S.T.G. acknowledges support from NASA award 80GSFC24CA067. A.C.S. acknowledges support from NOAA NA22OAR4310599, ONR ASTraL research initiative N00014-23-1-2092 and NASA 21-OSST21-0026. This work is based on S2S data. S2S is a joint initiative of the World Weather Research Programme (WWRP) and the World Climate Research Programme (WCRP). The original S2S database is hosted at ECMWF as an extension of the TIGGE database.

https://doi.org/10.5194/egusphere-2025-4142
Preprint. Discussion started: 10 September 2025

References

Alkhalidi, M., Al-Dabbous, A., Al-Dabbous, S., and Alzaid, D.: Evaluating the accuracy of the ERA5 model in predicting wind speeds across coastal and offshore regions, J. Mar. Sci. Eng., 13, 149, 2025.

Bernard, B., Madec, G., Penduff, T., Molines, J.-M., Treguier, A.-M., Le Sommer, J., Beckmann, A., Biastoch, A., Böning, C., Dengg, J., Derval, C., Durand, E., Gulev, S., Remy, E., Talandier, C., Theetten, S., Maltrud, M., McClean, J., and De Cuevas, B.: Impact of partial steps and momentum advection schemes in a global ocean circulation model at eddy-permitting resolution, Ocean Dyn., 56, 543–567, 2006.

Bishop, S. P., Justin Small, R., Bryan, F. O., and Tomas, R. A.: Scale Dependence of Midlatitude Air–Sea Interaction, J. Clim., 30, 8207–8221, 2017.

Bloom, S. C., Takacs, L. L., da Silva, A. M., and Ledvina, D.: Data assimilation using incremental analysis updates, Mon. Weather Rev., 124, 1256–1271, 1996.

Booth, J. F., Thompson, L., Patoux, J., and Kelly, K. A.: Sensitivity of midlatitude storm intensification to perturbations in the sea surface temperature near the Gulf Stream, Mon. Weather Rev., 140, 1241–1256, 2012.

Brassington, G. B., Martin, M. J., Tolman, H. L., Akella, S., Balmeseda, M., Chambers, C. R. S., Chassignet, E., Cummings, J. A., Drillet, Y., Jansen, P. A. E. M., Laloyaux, P., Lea, D., Mehra, A., Mirouze, I., Ritchie, H., Samson, G., Sandery, P. A., Smith, G. C., Suarez, M., and Todling, R.: Progress and challenges in short- to medium-range coupled prediction, J. Oper. Oceanogr., 8, s239–s258, 2015.

Buehner, M., McTaggart-Cowan, R., Beaulne, A., Charette, C., Garand, L., Heilliette, S., Lapalme, E., Laroche, S., Macpherson, S. R., Morneau, J., and Zadra, A.: Implementation of deterministic weather forecasting systems based on ensemble–variational data assimilation at Environment Canada. Part I: The global system, Mon. Weather Rev., 143, 2532–2559, 2015.

Cassou, C.: Intraseasonal interaction between the Madden-Julian Oscillation and the North Atlantic Oscillation, Nature, 455, 523–527, 2008.

Chen, T.-C., Collet, F., and Di Luca, A.: Evaluation of ERA5 precipitation and 10-m wind speed associated with extratropical cyclones using station data over North America, Int. J. Climatol., 44, 729–747, 2024.

Côté, J., Desmarais, J.-G., Gravel, S., Méthot, A., Patoine, A., Roch, M., and Staniforth, A.: The operational CMC–MRB global environmental multiscale (GEM) model. Part II: Results, Mon. Weather Rev., 126, 1397–1418, 1998a.

Côté, J., Gravel, S., Méthot, A., Patoine, A., Roch, M., and Staniforth, A.: The operational CMC–MRB global environmental multiscale (GEM) model. Part I: Design considerations and formulation, Mon. Weather Rev., 126, 1373–1395, 1998b.

DeMott, C. A., Klingaman, N. P., and others: Atmosphere-ocean coupled processes in the Madden-Julian oscillation, Reviews of, 2015.

Deng, X., Gagnon, N., Houtekamer, P. L., Beauregard, S., Chouinard, S., Aider, R., Charron, M., Fontecilla, J. S., Frenette, R., and Lahlou, R.: Improvements to the Global Ensemble Prediction System (GEPS) from version 4.3.0 to version 5.0.0. Meteorological Service of Canada, Environment and Climate Change Canada, Environment Canada, Centre Météorologique Canadien, division du développement, Tech. rep., 2018.

Fillion, L., Mitchell, H. L., Ritchie, H., and Staniforth, A.: The impact of a digital filter finalization technique in a global data assimilation system, Tellus A, 47, 304–323, 1995.

Gagnon, N., Deng, X.-X., Houtekamer, P., Beauregard, S., Erfani, A., Charron, M., Lahlou, R., and Marcoux, J.: Improvements to the global ensemble prediction system (GEPS) from version 3.1.1 to version 4.0.0. Meteorological service of Canada, environment and Climate Change Canada, environment Canada, centre météorologique canadien, division Du développement, Tech. Rep., 2014.

Gimeno, L., Nieto, R., Vázquez, M., and Lavers, D.: Atmospheric rivers: a mini-review, Front Earth Sci. Chin., 2, 2, 2014.

https://doi.org/10.5194/egusphere-2025-4142
Preprint. Discussion started: 10 September 2025

Girard, C., Plante, A., Desgagné, M., McTaggart-Cowan, R., Côté, J., Charron, M., Gravel, S., Lee, V., Patoine, A., Qaddouri, A., Roch, M., Spacek, L., Tanguay, M., Vaillancourt, P. A., and Zadra, A.: Staggered vertical discretization of the Canadian environmental multiscale (GEM) model using a coordinate of the log-hydrostatic-pressure type, Mon. Weather Rev., 142, 1183–1196, 2014.

Guan, B. and Waliser, D. E.: Detection of atmospheric rivers: Evaluation and application of an algorithm for global studies, J. Geophys. Res., 120, 12 514–12 535, 2015.

Hersbach, H., Bell, B., Berrisford, P., Hirahara, S., Horányi, A., Muñoz Sabater, J., Nicolas, J., Peubey, C., Radu, R., Schepers, D., Simmons, A., Soci, C., Abdalla, S., Abellan, X., Balsamo, G., Bechtold, P., Biavati, G., Bidlot, J., Bonavita, M., Chiara, G., Dahlgren, P., Dee, D., Diamantakis, M., Dragani, R., Flemming, J., Forbes, R., Fuentes, M., Geer, A., Haimberger, L., Healy, S., Hogan, R. J., Hólm, E., Janisková, M., Keeley, S., Laloyaux, P., Lopez, P., Lupu, C., Radnoti, G., Rosnay, P., Rozum, I., Vamborg, F., Villaume, S., and Jean-Noël Thépaut: The ERA5 global reanalysis, Quart. J. Roy. Meteor. Soc., 146, 1999–2049, 2020.

Higgins, T. B., Subramanian, A. C., Chapman, W. E., Lavers, D. A., and Winters, A. C.: Subseasonal Potential Predictability of Horizontal Water Vapor Transport and Precipitation Extremes in the North Pacific, Weather Forecast., 39, 833–846, 2024.

Hoskins, B. J. and Karoly, D. J.: The steady linear response of a spherical atmosphere to thermal and orographic forcing, J. Atmos. Sci., 38, 1179–1196, 1981.

Houtekamer, P. L., Mitchell, H. L., and Deng, X.: Model error representation in an operational ensemble Kalman filter, Mon. Weather Rev., 137, 2126–2143, 2009.

Houtekamer, P. L., Deng, X., Mitchell, H. L., Baek, S.-J., and Gagnon, N.: Higher resolution in an operational ensemble Kalman filter, Mon. Weather Rev., 142, 1143–1162, 2014.

Houtekamer, P. L., Buehner, M., and De La Chevrotière, M.: Using the hybrid gain algorithm to sample data assimilation uncertainty, Q. J. R. Meteorol. Soc., 145, 35–56, 2019.

Hsu, T.-Y., Mazloff, M. R., Gille, S. T., Freilich, M. A., Sun, R., and Cornuelle, B. D.: Response of sea surface temperature to atmospheric rivers, Nat. Commun., 15, 1–10, 2024.

Hunke, E. C.: Viscous–plastic sea ice dynamics with the EVP model: Linearization issues, J. Comput. Phys., 170, 18–38, 2001.

Hunke, E. C., Lipscomb, W. H., Turner, A. K., Jeffery, N., and Elliott, S.: CICE: the Los Alamos Sea Ice Model Documentation and Software User's Manual Version 5.0 LA-CC-06-012, https://citeseerx.ist.psu.edu/document?repid=rep1&type=pdf&doi=5eca93a8fbc716474f8fd80c804319b630f90316, accessed: 2025-3-30, 2015.

Karoly, D. J.: Rossby wave propagation in a barotropic atmosphere, Dyn. Atmos. Oceans, 7, 111–125, 1983.

Kiladis, G. N., Dias, J., Straub, K. H., Wheeler, M. C., Tulich, S. N., Kikuchi, K., Weickmann, K. M., and Ventrice, M. J.: A comparison of OLR and circulation-based indices for tracking the MJO, Mon. Weather Rev., 142, 1697–1715, 2014.

Kobashi, F., Doi, H., and Iwasaka, N.: Sea surface cooling induced by extratropical cyclones in the subtropical north pacific: Mechanism and interannual variability, J. Geophys. Res. Oceans, 124, 2179–2195, 2019.

Lin, H., Brunet, G., and Derome, J.: An observed connection between the North Atlantic Oscillation and the Madden-Julian oscillation, Journal of Climate, 22, 364–380, 2009.

Lin, H., Gagnon, N., Beauregard, S., Muncaster, R., Markovic, M., Denis, B., and Charron, M.: GEPS-Based Monthly Prediction at the Canadian Meteorological Centre, Mon. Weather Rev., 144, 4867–4883, 2016.

Lin, H., Deng, X., Peterson, A., Fontecilla, J. S., Smith, G., Muncaster, R., and Charron: Upgrade of the Global Ensemble Prediction System (GEPS) from version 5.0. 0 to version 6.0. 0. Meteorological Service of Canada, Environment and Climate Change Canada, Environment Canada, Centre Météorologique Canadien, division du développement, 2019.

https://doi.org/10.5194/egusphere-2025-4142
Preprint. Discussion started: 10 September 2025

Lipscomb, W. H., Hunke, E. C., Maslowski, W., and Jakacki, J.: Ridging, strength, and stability in high-resolution sea ice models, J. Geophys. Res. Oceans, 112, 2007.

Liu, X., Ma, X., Chang, P., Jia, Y., Fu, D., Xu, G., Wu, L., Saravanan, R., and Patricola, C. M.: Ocean fronts and eddies force atmospheric rivers and heavy precipitation in western North America, Nat. Commun., 12, 1268, 2021.

Madden, R. A. and Julian, P. R.: Detection of a 40–50 day oscillation in the zonal wind in the tropical pacific, J. Atmos. Sci., 28, 702–708, 1971.

Madec, G.: NEMO reference manual, ocean dynamics component: NEMO-OPA, Preliminary version. Note du Pole de modélisation, Institut Pierre-Simon Laplace (IPSL), France, 27, 1288–1161, 2008.

Molina, M. O., Gutiérrez, C., and Sánchez, E.: Comparison of ERA5 surface wind speed climatologies over Europe with observations from the HadISD dataset, Int. J. Climatol., 41, 4864–4878, 2021.

Pasquier, J. T., Pfahl, S., and Grams, C. M.: Modulation of atmospheric river occurrence and associated precipitation extremes in the North Atlantic region by European weather regimes, Geophys. Res. Lett., 46, 1014–1023, 2019.

Penny, S. G.: The hybrid local ensemble transform Kalman filter, Mon. Weather Rev., 142, 2139–2149, 2014.

Peterson, K. A., Smith, G. C., Lemieux, J.-F., Roy, F., Buehner, M., Caya, A., Houtekamer, P. L., Lin, H., Muncaster, R., Deng, X., Dupont, F., Gagnon, N., Hata, Y., Martinez, Y., Fontecilla, J. S., and Surcel-Colan, D.: Understanding sources of Northern Hemisphere uncertainty and forecast error in a medium-range coupled ensemble sea-ice prediction system, Quart. J. Roy. Meteor. Soc., 148, 2877–2902, 2022.

Polichtchouk, I., Mogensen, K. S., Sanabia, E. R., Jayne, S. R., Magnusson, L., Densmore, C. R., Hatfield, S., Hadade, I., Wedi, N., Anantharaj, V., Lopez, P., and Ekholm, A. K.: Effects of atmosphere and ocean horizontal model resolution on tropical cyclone and upper ocean response forecasts in four major hurricanes, Mon. Weather Rev., -1, 2025.

Qaddouri, A. and Lee, V.: The Canadian Global Environmental Multiscale model on the Yin-Yang grid system: Canadian GEM model on the Yin-Yang grid, Q. J. R. Meteorol. Soc., 137, 1913–1926, 2011.

Rainaud, R., Brossier, C. L., Ducrocq, V., and Giordani, H.: High-resolution air–sea coupling impact on two heavy precipitation events in the Western Mediterranean, Quart. J. Roy. Meteor. Soc., 143, 2448–2462, 2017.

Renault, L., Arsouze, T., Desbiolles, F., and Small, J.: Rectification effects of regional air-sea interactions over western boundary current on large-scale sea surface temperature and extra-tropical storm tracks, Sci. Rep., 14, 31 771, 2024.

Rutz, J. J., James Steenburgh, W., and Martin Ralph, F.: Climatological Characteristics of Atmospheric Rivers and Their Inland Penetration over the Western United States, Mon. Weather Rev., 142, 905–921, 2014.

Savarin, A. and Chen, S. S.: Pathways to better prediction of the MJO: 2. Impacts of atmosphere-ocean coupling on the upper ocean and MJO propagation, J. Adv. Model. Earth Syst., 14, e2021MS002 929, 2022.

Scaife, A. A., Comer, R. E., Dunstone, N. J., Knight, J. R., Smith, D. M., MacLachlan, C., Martin, N., Peterson, K. A., Rowlands, D., Carroll, E. B., Belcher, S., and Slingo, J.: Tropical rainfall, Rossby waves and regional winter climate predictions: Winter Teleconnections, Q. J. R. Meteorol. Soc., 143, 1–11, 2017.

Seo, H., O'Neill, L. W., Bourassa, M. A., Czaja, A., Drushka, K., Edson, J. B., Fox-Kemper, B., Frenger, I., Gille, S. T., Kirtman, B. P., Minobe, S., Pendergrass, A. G., Renault, L., Roberts, M. J., Schneider, N., Justin Small, R., Stoffelen, A., and Wang, Q.: Ocean Mesoscale and Frontal-Scale Ocean–Atmosphere Interactions and Influence on Large-Scale Climate: A Review, J. Clim., 36, 1981–2013, 2023.

Small, R. J., deSzoeke, S. P., Xie, S. P., O'Neill, L., Seo, H., Song, Q., Cornillon, P., Spall, M., and Minobe, S.: Air–sea interaction over ocean fronts and eddies, Dyn. Atmos. Oceans, 45, 274–319, 2008.

https://doi.org/10.5194/egusphere-2025-4142
Preprint. Discussion started: 10 September 2025

Smith, G. C., Bélanger, J.-M., Roy, F., Pellerin, P., Ritchie, H., Onu, K., Roch, M., Zadra, A., Colan, D. S., Winter, B., Fontecilla, J.-S., and Deacu, D.: Impact of Coupling with an Ice–Ocean Model on Global Medium-Range NWP Forecast Skill, Mon. Weather Rev., 146, 1157–1180, 2018.

Stan, C., Straus, D. M., Frederiksen, J. S., Lin, H., Maloney, E. D., and Schumacher, C.: Review of tropical-extratropical teleconnections on intraseasonal time scales, Rev. Geophys., 55, 902–937, 2017.

Subramanian, A. C., Balmaseda, M. A., Centurioni, L., Chattopadhyay, R., Cornuelle, B. D., DeMott, C., Flatau, M., Fujii, Y., Giglio, D., Gille, S. T., Hamill, T. M., Hendon, H., Hoteit, I., Kumar, A., Lee, J.-H., Lucas, A. J., Mahadevan, A., Matsueda, M., Nam, S., Paturi, S., Penny, S. G., Rydbeck, A., Sun, R., Takaya, Y., Tandon, A., Todd, R. E., Vitart, F., Yuan, D., and Zhang, C.: Ocean Observations to Improve Our Understanding, Modeling, and Forecasting of Subseasonal-to-Seasonal Variability, Frontiers in Marine Science, 6, 2019.

Sun, R., Cobb, A., Villas Bôas, A. B., Langodan, S., and others: Waves in SKRIPS: WaveWatch III coupling implementation and a case study of cyclone Mekunu, 2022.

Vellinga, M., Copsey, D., Graham, T., Milton, S., and Johns, T.: Evaluating benefits of two-way ocean–atmosphere coupling for global NWP forecasts, Weather Forecast., 35, 2127–2144, 2020.

Vitart, F., Buizza, R., Alonso Balmaseda, M., Balsamo, G., Bidlot, J.-R., Bonet, A., Fuentes, M., Hofstadler, A., Molteni, F., and Palmer, T. N.: The new VarEPS-monthly forecasting system: A first step towards seamless prediction, Quart. J. Roy. Meteor. Soc., 134, 1789–1799, 2008.

Vitart, F., Ardilouze, C., Bonet, A., Brookshaw, A., Chen, M., Codorean, C., Déqué, M., Ferranti, L., Fucile, E., Fuentes, M., Hendon, H., Hodgson, J., Kang, H.-S., Kumar, A., Lin, H., Liu, G., Liu, X., Malguzzi, P., Mallas, I., Manoussakis, M., Mastrangelo, D., MacLachlan, C., McLean, P., Minami, A., Mladek, R., Nakazawa, T., Najm, S., Nie, Y., Rixen, M., Robertson, A. W., Ruti, P., Sun, C., Takaya, Y., Tolstykh, M., Venuti, F., Waliser, D., Woolnough, S., Wu, T., Won, D.-J., Xiao, H., Zaripov, R., and Zhang, L.: The Subseasonal to Seasonal (S2S) Prediction Project Database, Bull. Am. Meteorol. Soc., 98, 163–173, 2017.

Waliser, D. and Guan, B.: Extreme winds and precipitation during landfall of atmospheric rivers, Nat. Geosci., 10, 179–183, 2017.

Wheeler, M. C. and Hendon, H. H.: An all-season real-time multivariate MJO index: Development of an index for monitoring and prediction, Mon. Weather Rev., 132, 1917–1932, 2004.

Winters, A. C.: Subseasonal prediction of the state and evolution of the north pacific jet stream, J. Geophys. Res., 126, 2021.

Yao, L., Lu, J., Xia, X., Jing, W., and Liu, Y.: Evaluation of the ERA5 sea surface temperature around the Pacific and the Atlantic, IEEE Access, 9, 12 067–12 073, 2021.

Zhu, Y. and Newell, R. E.: Atmospheric rivers and bombs, Geophys. Res. Lett., 21, 1999–2002, 1994.

Zuo, H., Balmaseda, M. A., and Mogensen, K.: The new eddy-permitting ORAP5 ocean reanalysis: description, evaluation and uncertainties in climate signals, Clim. Dyn., 49, 791–811, 2017.

https://doi.org/10.5194/egusphere-2025-4142
Preprint. Discussion started: 10 September 2025

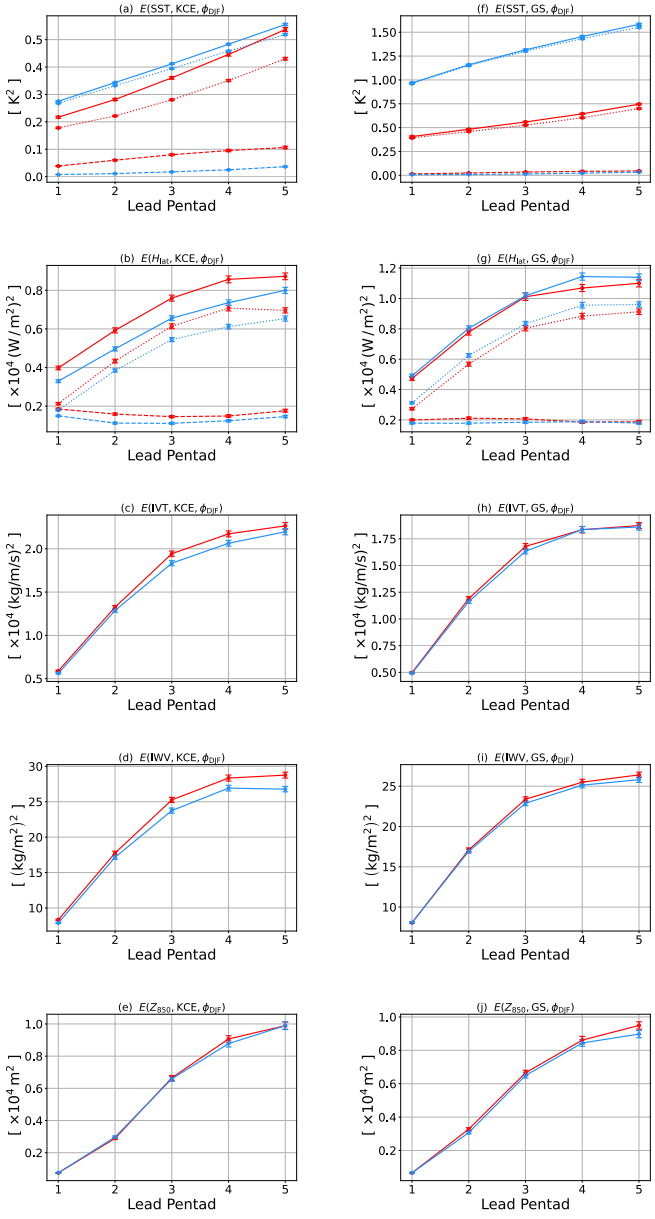

Figure 5. Bias variance E analysis of quantities as a function of pentads 1–6 computed from Global Ensemble Prediction System (GEPS) version 5 (GEPS5, red) to GEPS version 6 (GEPS6, blue) during December–January–February of the first three pentads in hindcast years 1998–2017. (a, f) sea surface temperature (SST). (b, g) Latent heat flux (H_{lat}. (c, h) Integrated vapor transport (IVT). (d, i) Integrated water vapor (IWV). (e, j) 850 hPa geopotential height Z_{850}. For SST (a and f) and H_{lat} (b and g), the decomposition of E into mean ($\overline{E}$, dashed) and patterned ($\tilde{E}$, dotted) variances are added. Panels a–e are for the Kuroshio Current Extension (KCE) region, and f–j are for Gulf Stream (GS) region. The whiskers represent the standard error.

https://doi.org/10.5194/egusphere-2025-4142
Preprint. Discussion started: 10 September 2025

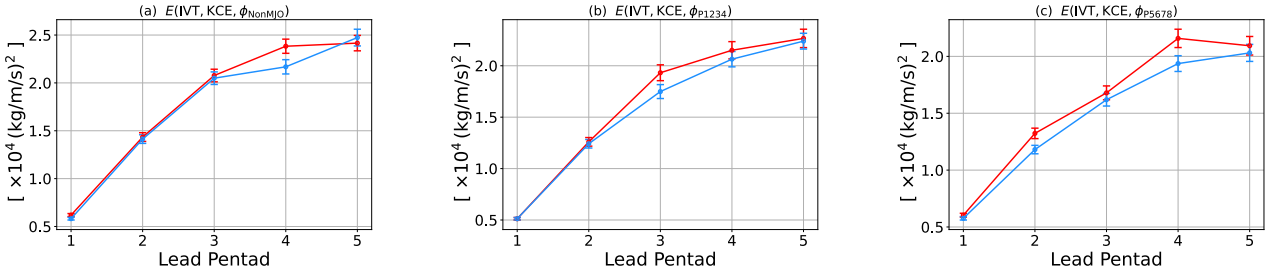

Figure 6. Bias variance E analysis of integrated vapor transport (IVT) as a function of pentads 1–6 computed from Global Ensemble Prediction System (GEPS) version 5 (GEPS5, red) to GEPS version 6 (GEPS6, blue) using different start time groups in hindcast years 1998–2017 for Kuroshio Current Extension region. (a) Non-MJO group. (b) P1234 group. (c) P5678 group. The whiskers represent the standard error.